Measurement 270 (2026) 120838

Contents lists available at ScienceDirect

Measurement

journal homepage: www.elsevier.com/locate/measurement

Decoupling atmospheric and multipath errors in NRTK landslide monitoring: A refined multipath modelling strategy

Xinrui Li [a,b], Xuanyu Qu [b,c,d,*], Xiaoli Ding [b,c,d], Wenkun Yu [e], Li Wang [a]

[a] College of Geological Engineering and Geomatics, Chang'an University, Xi'an 710054, China
[b] Department of Land Surveying and Geo-Informatics, The Hong Kong Polytechnic University, Hong Kong, China
[c] Research Institute for Land and Space, The Hong Kong Polytechnic University, Hong Kong, China
[d] Shenzhen Research Institute, The Hong Kong Polytechnic University, Shenzhen 518057, China
[e] School of Geosciences and Info-Physics, Central South University, Changsha 410083, China

ARTICLE INFO

Keywords:
NRTK
Landslide monitoring
Multipath mitigation
Atmospheric errors
Sidereal filtering

ABSTRACT

Network Real-Time Kinematic (NRTK) high-precision deformation monitoring is affected by the superposition of multipath effects and residual atmospheric delay. Unmodeled atmospheric errors can contaminate multipath correction models and degrade positioning accuracy if not properly separated. This study proposes a refined multipath mitigation method. First, Complementary Ensemble Empirical Mode Decomposition (CEEMD) is applied to suppress high-frequency white noise. Multichannel Singular Spectrum Analysis (MSSA) is then used to jointly decompose the denoised residuals from multiple Orbital Repetition Times (ORTs) and generate the corresponding Reconstructed Components (RCs). We then evaluate the temporal coherence of RCs across channels, components that exhibit high temporal similarity across ORTs are identified as multipath-related and are used for multipath modeling. Using data from the Hong Kong SatRef network, including various Virtual Reference Station (VRS) baseline lengths and an ultra-short baseline scenario, we demonstrate significant improvements in positioning accuracy and robustness across baselines. The proposed method consistently improved horizontal positioning by 9% and vertical positioning by 6% compared to a conventional three-day SF, and by 15–19% relative to unfiltered solutions. Moreover, heavy rainfall, as an important landslide trigger, was observed to amplify both multipath and atmospheric errors, temporarily reducing NRTK positioning accuracy.

1. Introduction

Global Navigation Satellite System (GNSS) positioning technique plays a crucial role in various deformation monitoring scenarios, landslide monitoring [1], seismology [2], and structural health monitoring of bridges [3]. Among existing GNSS positioning techniques, Real-Time Kinematic (RTK) positioning is widely adopted due to its high precision and instantaneous Ambiguity Resolution (AR). However, RTK usually requires to establish and maintain a local reference station for accurate deformation solutions, which increases monitoring cost [4]. With the development of Continuously Operating Reference Station (CORS), network-based RTK (NRTK) positioning has emerged as a solution that utilizes multiple reference stations to model distance-dependent errors, enabling high-accuracy, real-time positioning over large areas [5].

One of the most challenging error sources in NRTK positioning is multipath error, which cannot be directly eliminated through functional modeling, differencing, or observation combinations. Fortunately, for static or quasi-static GNSS stations, multipath errors exhibit strong spatial and temporal repeatability, making them amenable to targeted mitigation techniques. Two representative methods for multipath mitigation include the Sidereal Filtering (SF) [6] and Multipath Hemispherical Mapping (MHM) [7,8], which leverage the temporal and spatial characteristics of multipath errors, respectively. Temporal-domain methods extract multipath components from coordinate or observation residuals and apply Orbital Repeat Times (ORTs) to correct multipath errors in real time. Common multipath extraction techniques include low-pass filtering [9,10], Wavelet Transform (WT) [11–13], and Multichannel Singular Spectrum Analysis (MSSA) [14]. On the other hand, spatial-domain methods mitigate multipath by averaging [8] or modeling residuals [15,16] within a predefined grid to suppress high-frequency noise.

These methods rely on predefined spectral assumptions, that is, the

* Corresponding author at: Department of Land Surveying and Geo-Informatics, The Hong Kong Polytechnic University, Hong Kong, China.
E-mail address: xuany.qu@connect.polyu.hk (X. Qu).

https://doi.org/10.1016/j.measurement.2026.120838
Received 14 November 2025; Received in revised form 9 February 2026; Accepted 11 February 2026
Available online 16 February 2026

assumption that multipath and other unmodeled errors can be separable in the frequency domain. Such assumptions are valid in short-baseline RTK scenarios, where double-differencing largely eliminates most error sources and leaves only multipath and high-frequency noise in the residuals [17]. However, the large inter-station distances in CORS networks reduce the spatial correlation of atmospheric delays, resulting in less accurate atmospheric delay modelling [18]. Consequently, NRTK-derived Double Differenced (DD) residuals inevitably contain unmodeled atmospheric errors. Due to the spectral overlap between atmospheric and multipath errors, traditional filtering or spatial averaging approaches struggle to distinguish between these two error sources [19,20]. If atmospheric errors are not properly identified, they may be mistaken for multipath errors and ultimately degrade the performance of multipath corrections [21].

Current strategies for decoupling multipath errors and other unmodeled errors can be classified into two categories. The first strategy is to suppress other unmodeled errors before extracting the multipath errors. For example, Zheng et al. [22] exploited the spatiotemporal differences between Common-Mode Errors (CME) and multipath errors in regional GNSS networks. They applied Principal Component Analysis (PCA) to first extract CME from residuals, treating the remaining low-frequency residuals at each station as multipath errors. Other studies [23,24] have reduced tropospheric modeling errors by constructing precise tropospheric correction models during residual extraction. While such approaches can effectively mitigate specific types of unmodeled errors, their limitation lies in their specificity, only targeting particular error sources and leaving behind residual low-frequency errors that may still contain non-multipath components.

The second strategy leverages the pronounced temporal repeatability of multipath errors to isolate them from other unmodeled error sources. Geng et al. [19,20] demonstrated that averaging multipath errors extracted from multiple days can attenuate other unmodeled errors. This method leverages the assumption that other unmodeled errors generally lack temporal repeatability, making them susceptible to reduction through multi-day averaging. Dai et al. [25] and Yu et al. [26] applied PCA to residuals over several consecutive days, treating the principal components as multipath errors. This approach performs well in short-baseline RTK scenarios where multipath dominates the residuals. However, under NRTK conditions, the introduction of atmospheric errors reduces the relative significance of multipath errors, making it difficult for PCA to effectively distinguish multipath from atmospheric errors.

As a nonparametric and adaptive signal processing method, Complementary Ensemble Empirical Mode Decomposition (CEEMD) [27] decomposes time series into a set of Intrinsic Mode Functions (IMFs) and a residual term based on the inherent temporal scales of the data. It effectively addresses the mode mixing problems commonly encountered in EMD, while improving computational efficiency and enhancing the suppression of added white noise compared to EEMD. MSSA is another nonparametric spectral estimation technique widely used to extract periodic and long-term signals from multivariate time series[28].

In this study, we propose a novel approach to mitigate the contamination of multipath correction models by residual atmospheric delays. The proposed method exploits the intrinsic spatiotemporal differences between multipath and atmospheric errors, enabling the direct separation of multipath errors from observation residuals containing multiple error sources, without relying on predefined spectral assumptions or requiring multipath to dominate the signal energy. The effectiveness of the method is validated using real GNSS data from a landslide monitoring network in Hong Kong.

2. Methodology

This section theoretically analyzes the components of the DD residuals in NRTK and outlines the precise steps for extracting multipath errors from DD residuals that contain atmospheric errors.

2.1. The observation residuals components at the user-side of NRTK

After the server generates virtual observations based on the approximate coordinates near the monitoring station, these virtual observations, along with the corresponding coordinates, are transmitted to the designated user. Then, the DD observations is formed, which effectively eliminate errors associated with satellite orbits, satellite and receiver clock biases, as well as satellite and receiver hardware delays. However, in Virtual Reference Station (VRS) mode [5], the interpolated atmospheric information is directly applied to correct the observations, which imposes a strong atmospheric constraint and introduces atmospheric modeling errors. As a result, the DD residuals will not only contain multipath and observation noise but also ionospheric and tropospheric errors [29]. Therefore, the DD residuals can be expressed as,

$$\nabla\Delta P^{pq}_{AB,i} = \nabla\Delta\rho^{pq}_{AB} + \nabla\Delta I^{pq}_{AB} + \nabla\Delta T^{pq}_{AB} + \nabla\Delta M^{pq}_{AB,P,i} + \varepsilon_{P,i}$$

$$\nabla\Delta L^{pq}_{AB,i} = \nabla\Delta\rho^{pq}_{AB} - \nabla\Delta I^{pq}_{AB} + \nabla\Delta T^{pq}_{AB} + \nabla\Delta M^{pq}_{AB,L,i} + \varepsilon_{L,i} + \lambda\cdot\nabla\Delta N^{pq}_{AB,i} \quad (1)$$

where $\nabla\Delta$ is the DD operator. A and B indicate the monitoring and virtual reference station, respectively; and superscripts p and q denote the observed and reference satellites, respectively. i is the GNSS signal frequency number. ρ is the geometric distance form the satellite antenna phase centre to the receiver phase centre. I is the slant ionospheric delay. T denotes the troposphere delay. $M_P(\varepsilon_P)$ and M_L (ε_L) denote the multipath errors (observation noise) in pseudorange and phase, respectively. $\nabla\Delta N^{pq}_{AB,i}$ is the DD ambiguity.

When the exact receiver positions are known, the geometric range ρ can be easily calculated, and the DD integer ambiguity $\nabla\Delta N^{pq}_{AB,i}$ can also be resolved. To improve the ambiguity resolution fixed rate, a partial AR strategy was employed in this study [30]. When $\nabla\Delta\rho^{pq}_{AB}$ and $\nabla\Delta N^{pq}_{AB,i}$ are known, the DD pseudorange or phase residuals can be expressed as,

$$R^{pq}_{AB,i} = MP^{pq}_{AB,i} + ATM^{pq}_{AB,i} + \varepsilon_i \quad (2)$$

where $R^{pq}_{AB,i}$ represents the double difference residual. $MP^{pq}_{AB,i}$ and ε_i correspond to the multipath errors and observation noise in the residuals, respectively. $ATM^{pq}_{AB,i}$ represents the atmospheric errors caused by ionospheric and tropospheric modeling errors. To avoid the influence of changing reference satellites on the residuals, a "zero-mean" condition is used to separate the inter-station single-difference (SD) residuals $R^{p}_{AB,i}$ from $R^{pq}_{AB,i}$ [10]. The subsequent multipath extraction is based on the $R^{p}_{AB,i}$ residuals.

2.2. Decoupling multipath and atmospheric components

For static stations, multipath errors exhibit strong spatiotemporal repeatability, manifesting as consistent temporal patterns across ORTs, whereas atmospheric errors generally do not. Leveraging this property, we propose a refined multipath extraction method consisting of three main steps. First, CEEMD is applied to decompose the residuals into IMFs, which are then classified as either "noise only" or "signal + noise" modes. Second, MSSA is used to decompose the retained "signal + noise" residuals from multiple ORTs into a series of RCs. Multipath components are subsequently identified based on their inter-ORT temporal coherence. The detailed workflow of the proposed method is illustrated in Fig. 1.

Step 1: Data preprocessing and CEEMD-based high-frequency noise removal.

Since the subsequent identification of multipath and atmospheric errors relies on spatiotemporal patterns across multiple ORTs, denoising the residuals in advance improves the signal-to-noise ratio (SNR) and enhances the extraction of physically meaningful structures. CEEMD is applied to decompose the preprocessed SD residuals into n IMFs and a

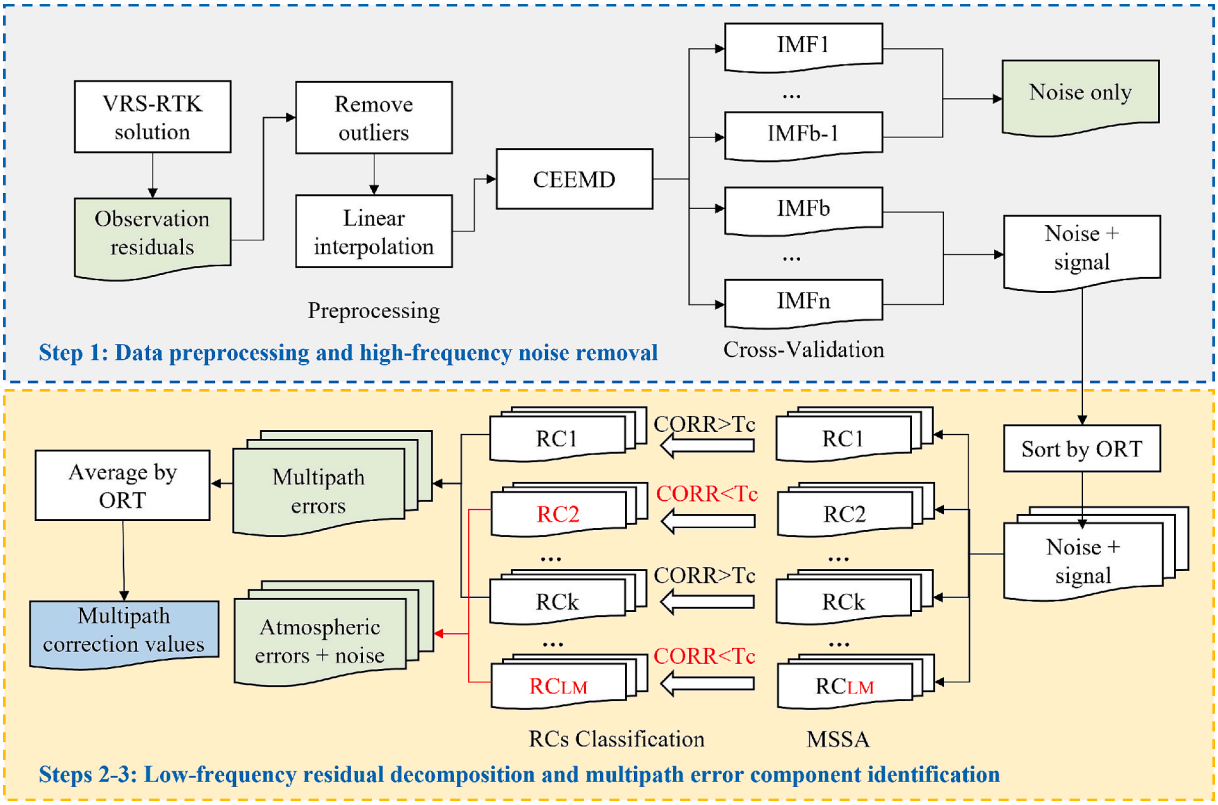

Fig. 1. Flowchart of refined multipath extraction method considering the influence of atmospheric errors.

residual term *res*. Cross-validation (CV) is then used to determine the optimal boundary layer b that minimizes the mean variance [31], thereby identifying the boundary between noise and signal components. To avoid discarding useful high-frequency multipath signals, IMF_1 to IMF_{b-1} are classified as "noise only" and discarded, while IMF_b to IMF_n are retained as "signal + noise" and reconstructed for the next step. For frequency i, this can be expressed as,

$$LOW_{AB}^{p} = CEEMD_{cv}(R_{AB}^{p}) = res + \sum_{i=b}^{n} IMF_i \tag{3}$$

where $1 \le b \le n$, and LOW_{AB}^{p} represents the "signal + noise" residuals after CEEMD filtering. Detailed settings for the CV method can be found in Zhong et al. [31] and Qu et al. [32]. For implementation simplicity, IMF_1 can also be directly removed as "noise only" as an alternative.

Step 2: Low-frequency residual decomposition based on MSSA.

We use the residuals from the first three ORTs to extract multipath errors, after alignment to the sidereal day, can be expressed as $LOW_{AB,l}^{p}(t)$ ($l = 1,2\cdots,L$; $t = 1,2,\ldots,N$), where t denotes the epoch index, N is the total number of epochs within one ORT for the satellite, and L is the number of ORT (with $L = 3$ in this case). For simplicity, we denote $LOW_{AB,l}^{p}(t)$ as $X_l(t)$; thus, we have,

$$X_3(t) = X_2(t + T_{ORT}) = X_1(t + 2T_{ORT}) \tag{4}$$

where T_{ORT} represents the orbital repetition time (for Global Positioning System (GPS) data with a 30-second epoch interval, T_{ORT} = 23 h 56 m [9]).

Next, the MSSA technique is adopted to decompose $X_l(t)$ into a series of RCs, which can be expressed as,

$$\left(\Lambda, \left[RC_1^k(t), RC_2^k(t), RC_3^k(t)\right]\right) = MSSA([X_1(t), X_2(t), X_3(t)])k = 1, 2, \cdots, LM \tag{5}$$

where Λ is the eigenvalue matrix arranged in descending order, i.e., $\Lambda = diag\left[\lambda^1, \lambda^2, \cdots, \lambda^k, \cdots, \lambda^{LM}\right]$, with $\lambda^1 > \lambda^2 > \cdots > \lambda^k > \cdots > \lambda^{LM}$. $RC_l^k(t)$ denotes the k-th reconstruction component of the l-th ORT, corresponding to λ^k; and M is the lag-window size, where $1 < M < N/2$. In this study, M is set to $(N+1)/(L+1)$, ensuring the trajectory matrix reaches maximal rank and enabling separation of distinct components [33]. For further details on the MSSA in Eq. (5), please refer to Eqs. (4)–(10) in Li et al. [14].

Each eigenvalue λ^k quantifies the energy contribution of the corresponding component across three channels, indicating how much of the original residuals fluctuations is represented by that component. Each RC triplet $\left[RC_1^k(t), RC_2^k(t), RC_3^k(t)\right]$ captures a specific spectral embedded in the multichannel time series, effectively representing different manifestations or projections of the same underlying dynamic process (e.g., multipath or atmospheric error) across multiple channels (i.e., different ORTs) [34].

Step 3: Multipath error identification based on distinct error characteristics.

Multipath errors, due to their inherent sidereal periodicity, tend to project similarly across ORTs, resulting in RCs that exhibit strong temporal coherence. In contrast, atmospheric errors generally lack such inter-ORT repeatability, leading to greater variability in their RCs across channels. Based on this difference, we propose a correlation-based strategy to distinguish multipath-related RCs. Specifically, we compute the Pearson correlation coefficient (PCC) for each k-th RC across all channel pairs. The selection criterion for multipath-related components is:

$$corr\left(RC_i^k(t), RC_j^k(t)\right) > T_c; \forall i \ne j; i, j = 1, 2, 3 \tag{6}$$

where T_c is the predetermined PCC threshold, which is set to $T_c = 0.6$ in this study. In practice, the multipath identification is only weakly sensitive to the choice of T_c value, because RCs typically exhibit either strong inter-ORT coherence or almost no correlation. To avoid inter-

ference from short-term pseudo-repetitive atmospheric signals[22], only the RCs satisfying the threshold condition across all three ORT pairs are retained as multipath components.

For the l-th ORT, the multipath and atmospheric errors are reconstructed from the selected RCs as:

$$\widehat{MP}^{\mathrm{p}}_{AB,l}(t) = \sum_{k\in K_t} RC^k_l(t)$$

$$\widehat{ATM}^{\mathrm{p}}_{AB,l}(t) = \sum_{k\in K_{no-t}} RC^k_l(t) \tag{7}$$

where K_t denote the index sets of RCs passing the correlation threshold. K_{no-t} represents the index set of RCs that do not meet the threshold and have corresponding eigenvalues greater than $0.9{*}\sum_{k=1}^{LM}\lambda^k$, in order to exclude the influence of residual white noise. Finally, we apply the sidereal filtering (SF) method by averaging the $\widehat{MP}^{\mathrm{p}}_{AB,l}$ for $l = 1, 2, 3$ to obtain the corresponding multipath correction value. This makes the proposed method fundamentally different from conventional filtering approaches that rely on predefined spectral separability between multipath and other errors. Instead, it identifies multipath based on the distinct spatiotemporal behaviors of different error sources, allowing effective separation even when multipath is not the dominant component in the residuals.

To quantify the contribution of multipath or atmospheric error to the residuals, we define their relative energy ratio R_X as the sum of their associated eigenvalues normalized by the total eigenvalue sum across all RCs,

$$R_X = \sum_{k\in S_X}\lambda^k \Big/ \sum_{k=1}^{LM}\lambda^k,\ S_X \in \{K_t, K_{no-t}\} \tag{8}$$

3. Results and analysis

To validate the proposed method, we collected datasets from a monitoring station and a local reference station in a real-world landslide area. The observations from DOY 1 to DOY 15, 2023 are adopted. In addition, eight CORS stations from the Hong Kong Satellite Positioning Reference Station Network (SatRef) are also collected to calculate VRS-RTK solutions (Fig. 2a). In order to evaluate the performance of the proposed method under networks with different sizes, two calculation schemes were designed.

- **Scheme 1**: The VRS observations are generated by the observation of the CORS station with an average inter-station distance of approximately 13 km, denoted as short-baseline VRS (SVRS);
- **Scheme 2**: The VRS observations are generated by the observation of the CORS station with an average inter-station distance of approximately 29 km, denoted as long-baseline VRS (LVRS).

For comparative verification, we also utilized data from a locally established reference station (REFE) with a baseline length of only 100 m to form an ultra-short baseline RTK (SRTK) solution. The location of the monitoring station (SA02) and the REFE station are shown in Fig. 2b. Fig. 2c, 2d, and 2e display the environmental conditions in the vicinity of the SA02 and REFE stations, where dense vegetation and significant obstructions are evident; detailed information on the environment surrounding the CORS stations can be found at https://www.geodetic.gov.hk/en/index.htm. During the experiments, dual-frequency GPS and BeiDou-2 Navigation Satellite System (BDS-2) observation data were used, with an epoch interval of 30 s.

3.1. Multipath errors extraction under NRTK

We selected data from DOY 5 to DOY 7 as an example. Fig. 3 shows the phase and pseudorange residuals for satellites G05 and C06 at station SA02 over three consecutive ORTs calculated using SVRS and LVRS schemes. As the network baseline length increases, the inter-ORT correlations of the carrier phase residuals for both satellites decreases significantly, indicating increased atmospheric errors at the monitoring station.

Fig. 4a presents the CEEMD decomposition results of the phase residuals for satellite G05 in ORT3 under the LVRS scheme, along with the corresponding Fast Fourier Transform (FFT) spectra. It can be observed that IMF1 mainly contains high-frequency white noise, while IMF2 exhibits a mixture of noise and low-to-mid frequency signals. Fig. 4b shows the variance mean values when selecting IMF1 to IMF7 as the cutoff IMF. The minimum mean variance is reached at IMF2, indicating it as the optimal boundary between noise and signal. Therefore, IMF1 is classified as the "noise only" component, and IMF2 to IMF7 are considered "signal + noise" components, which are retained for subsequent multipath error extraction.

We then apply the MSSA to the CEEMD denoised residuals to obtain a series RCs. Fig. 5(a) and (b) show the first eight RCs and their corresponding FFTs for the G05 and C06 satellites, respectively. The RC that pass or fail to pass the criteria Eq. (6) are depicted in black and red, respectively. For example, for the G05 phase residuals, RC3 fulfills the threshold requirement for all ORTs, while RC4 in ORT3 does not. Consequently, RC3 is classified as a multipath component, whereas RC4 is excluded from the multipath modeling.

Fig. 6 compares the multipath errors extracted using the traditional CEEMD approach (i.e., discarding the boundary IMF and treating the remaining IMFs as multipath) with those obtained using the proposed

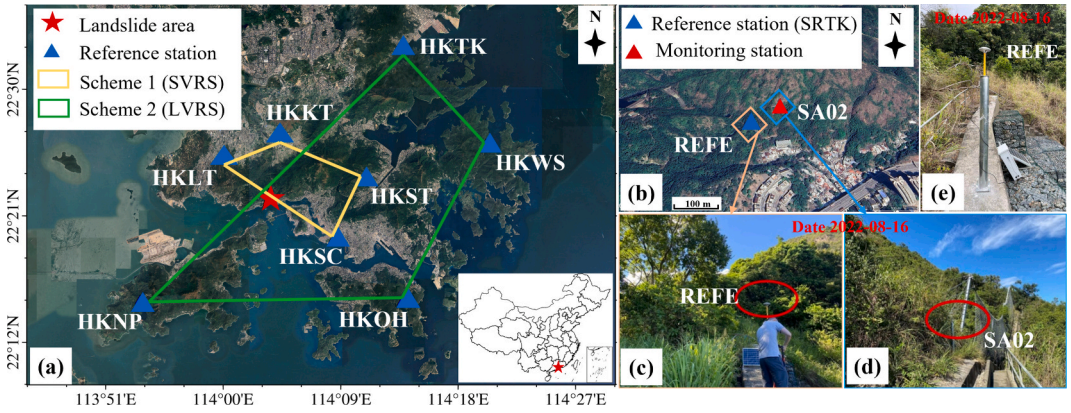

Fig. 2. Overview of the study area. **a** Distribution of SVRS and LVRS schemes, along with the location of the landslide area. **b** Locations of the REFE reference station and the monitoring station (SA02). **c** and **d** Surrounding environments of the REFE and SA02 stations. **e** Installation example of the REFE station.

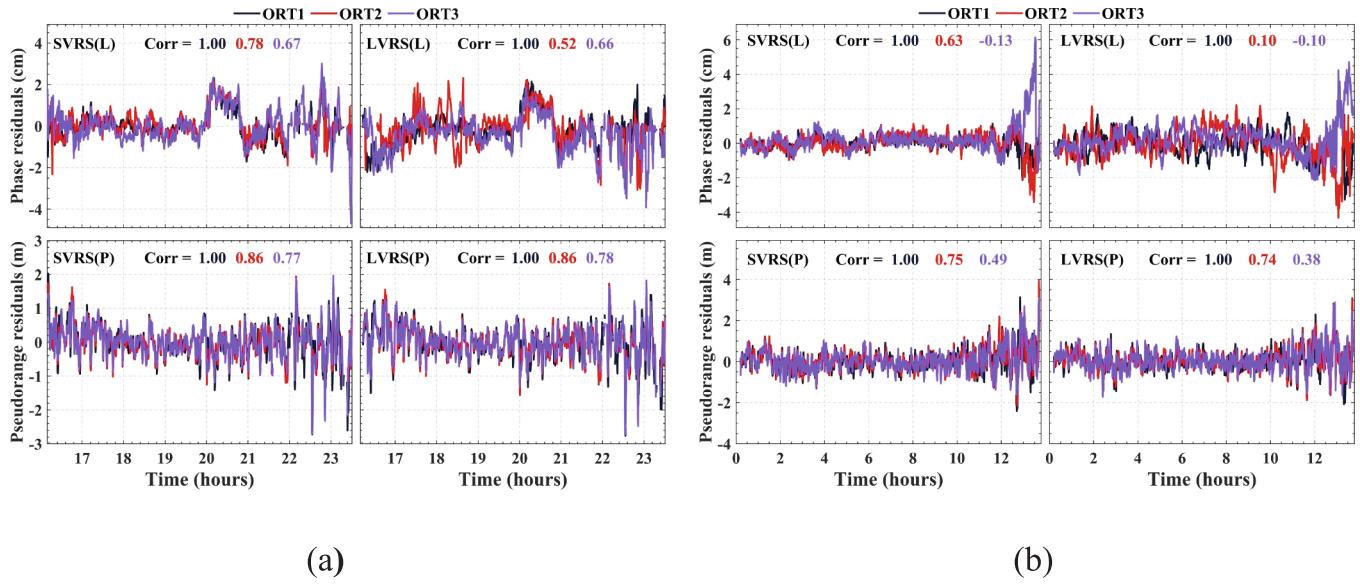

Fig. 3. Phase (L) and pseudorange (P) residuals calculated for **a** G05 and **b** C06 satellites at SA02 station under SVRS and LVRS schemes, computed over three consecutive ORTs. The correlation coefficients (Corr) compare each ORT's residuals to those of ORT1.

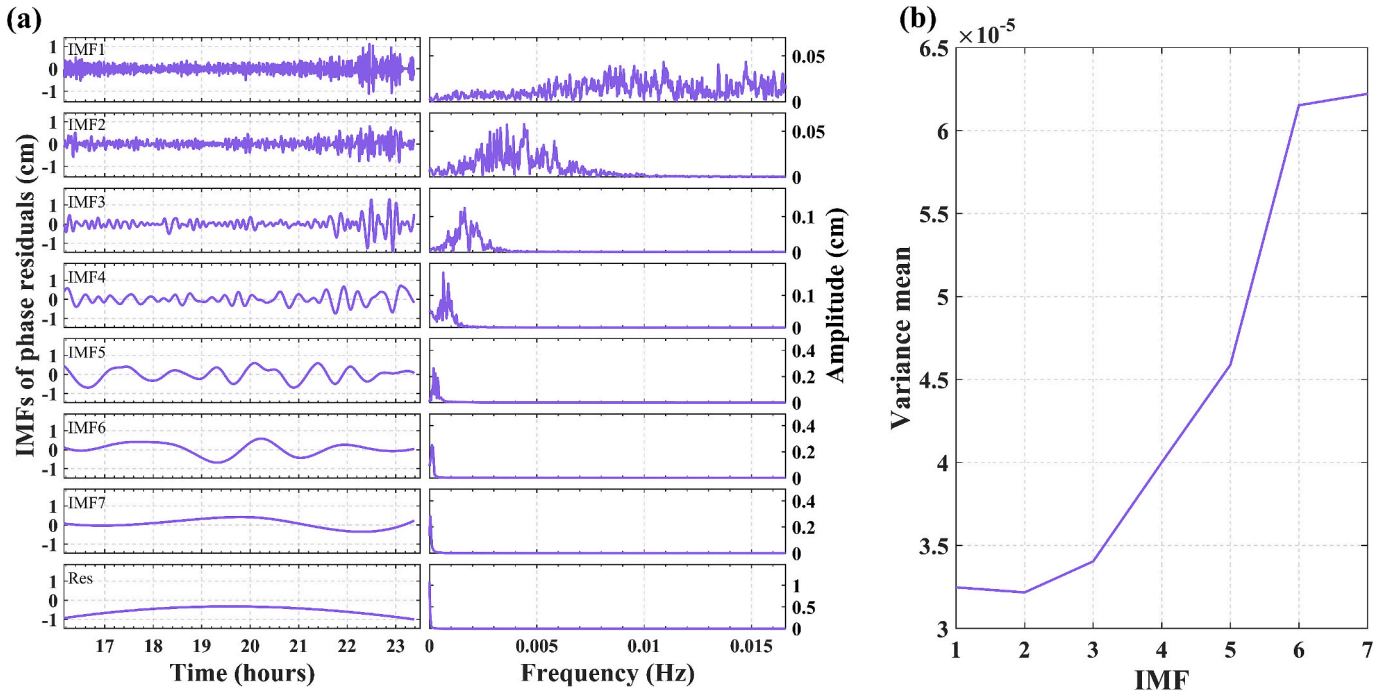

Fig. 4. A CEEMD decomposition (left column) and corresponding FFT (right column) of the carrier phase residuals for satellite G05 in ORT3 (LVRS scheme); **b** variance mean values corresponding to different cutoff IMFs.

method. Compared to the CEEMD-only approach, the proposed method more effectively suppresses non-repetitive atmospheric components in the low-frequency residuals. Moreover, comparison of the pseudorange residuals before and after final reconstruction reveals that our method better preserves high-frequency multipath features.

For C06, the recovered multipath amplitudes are smaller. This is primarily attributed to the less stable ORT of BDS Inclined Geo-Synchronous orbit (IGSO) satellites, which weaken the inter-ORT coherence of multipath [35]. In addition, the atmospheric modeling and interpolation accuracy of the BDS-2 system is generally lower than that of GPS, resulting in more pronounced atmospheric errors in the BDS phase residuals [36]. As a result, the partial RCs derived by MSSA does not completely separate multipath and atmospheric errors. These mixed components fail to meet the correlation criterion in Eq. (6), and therefore only the strongly coherent multipath components are finally retained.

We use data from DOY 5 to DOY 7 to build four different multipath correction models, and then apply to the data from DOY 8 for multipath mitigation with SF technique. The four multipath extraction and SF model construction are as follows: unfiltered (M0), Multipath extraction using single ORT data with CEEMD denoising (M1), Multipath extraction by averaging three ORTs data with CEEMD denoising (M2, [20],

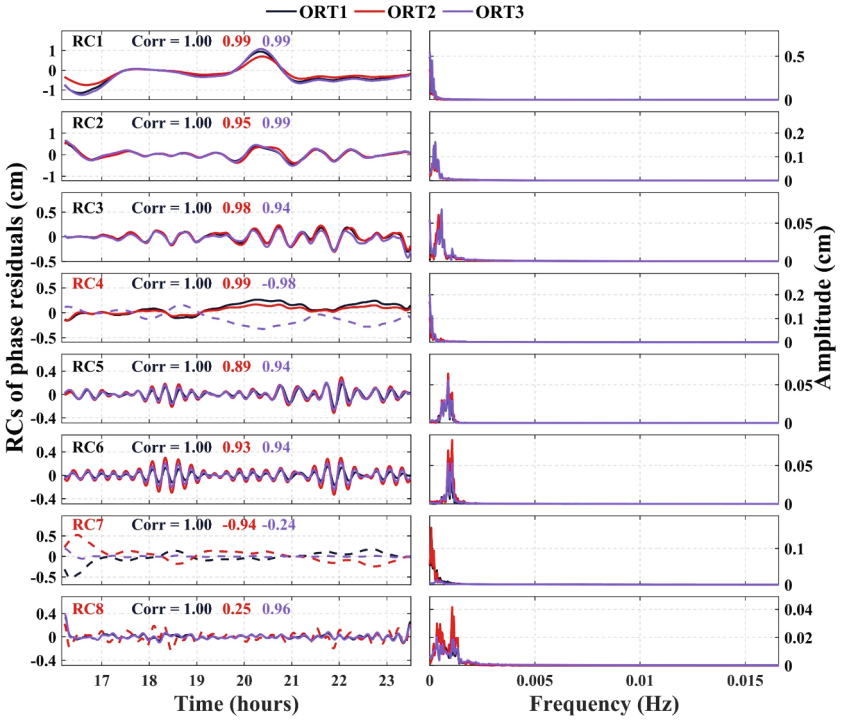

(a)

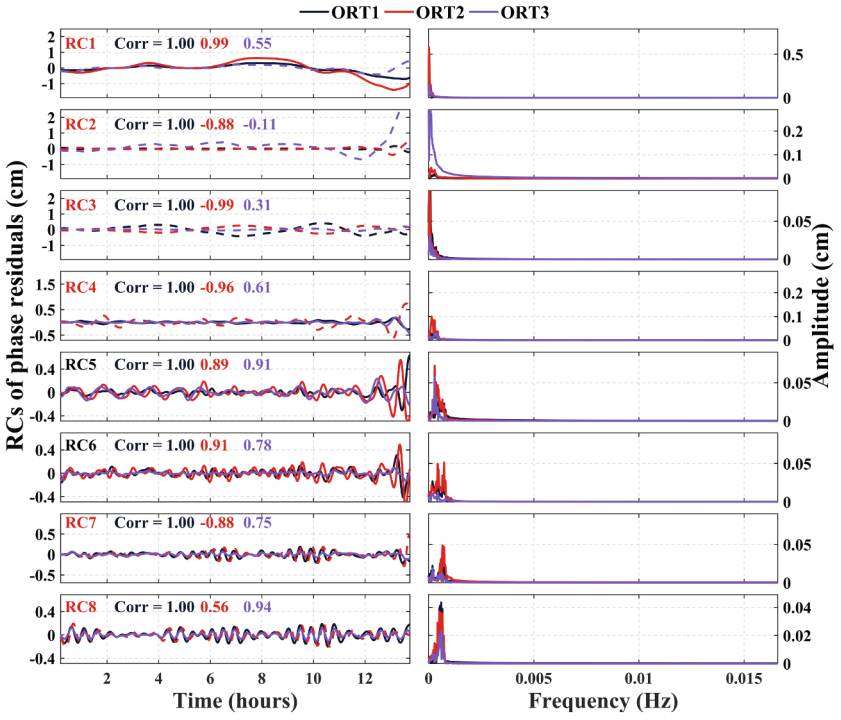

(b)

Fig. 5. The first eight RCs (left column) and their FFT (right column) of the **a** G05 and **b** C06 satellites phase residuals after MSSA decomposition under the LVRS scheme. The multipath components are marked. The colored correlation coefficients (Corr) refer to each RC's correlation with the reference ORT.

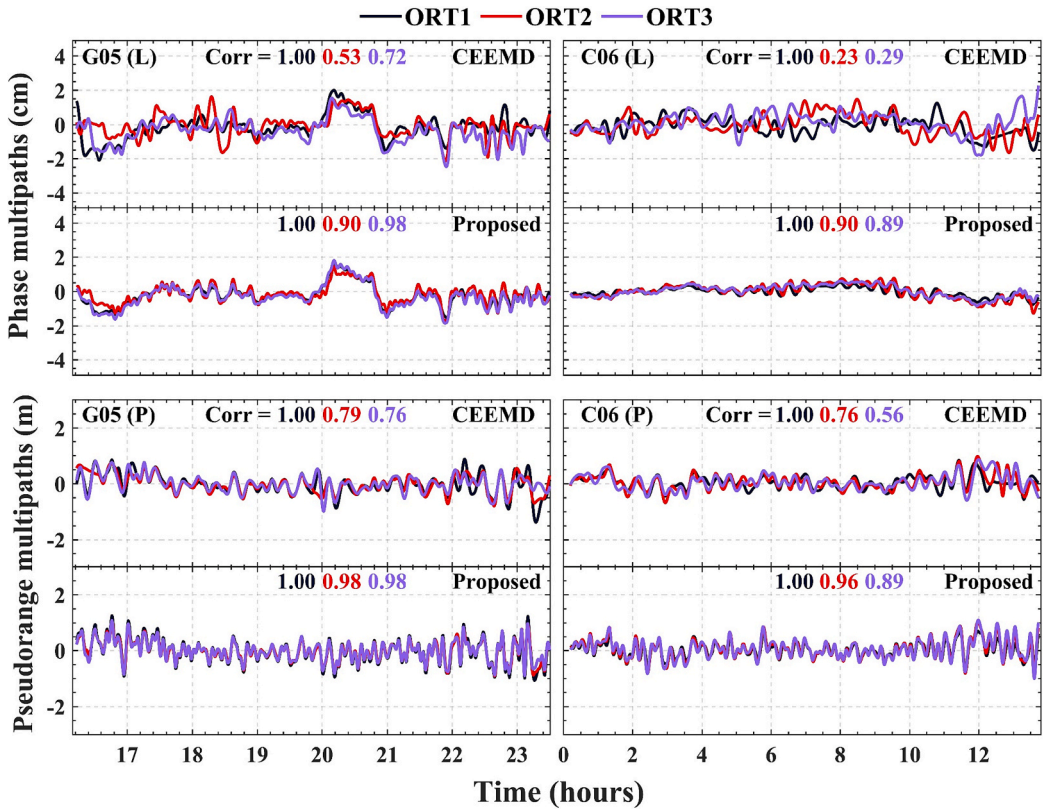

Fig. 6. Phase and pseudorange multipath errors for G05 (left column) and C06 (right column) satellites under the LVRS scheme, obtained by the traditional CEEMD and proposed methods. The correlation coefficients of the multipath errors for each ORT relative to ORT1 were computed.

Multipath extraction by combine CEEMD and PCA to extract principal components (M3, [26], and proposed method (M4). Fig. 7 illustrates the phase residual Power Spectral Density (PSD) for G05 and C06 under the LVRS scheme, before and after multipath correction. In the mid-frequency band (200 s to 2,000 s wavelength), all four methods effectively mitigate multipath errors. However, in the low-frequency band (less than 2,000 s wavelength), atmospheric errors become more notable, leading to noticeable low-frequency deviations for C06 in M1 and M3. The proposed method demonstrates better performance in handling such low-frequency atmospheric components.

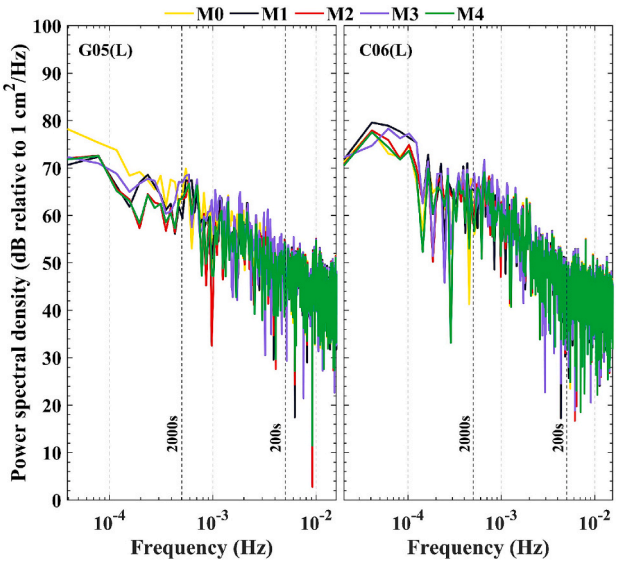

Fig. 7. Phase residual PSD for satellites G05 (left column) and C06 (right column) at station SA02 under the LVRS scheme with different multipath correction strategies.

3.2. *Impact of multipath mitigation on positioning accuracy*

Fig. 8 shows the original Root Mean Square (RMS) positioning errors at station SA02 on DOY 8 under three different solutions (SRTK, SVRS, LVRS), as well as the results after applying four multipath mitigation methods (M1–M4). Under the SRTK scheme, the four multipath mitigation methods (M1–M4) exhibit similar correction performance. This is because the DD residuals contain only multipath and observation noise, allowing each filtering approach to effectively remove high-frequency noise, leaving only multipath errors in the final correction model. However, with the SVRS and LVRS solutions, the DD residuals still include atmospheric errors. The conventional M1 method cannot effectively remove these errors, leading to a significant "negative optimization" in the east component after multipath correction. Compared to M1, the M2 and M3 methods partially mitigate atmospheric errors, but as the baseline length increases (from SVRS to LVRS), their effectiveness gradually weakens, causing deterioration in the corrected results. In contrast, the proposed M4 method avoids introducing atmospheric errors into the multipath correction model and thus achieves robust correction performance across all three baseline lengths.

Fig. 8 also reveals that although the baseline for SRTK is merely 100 m, its raw positioning accuracy is lower than that of SVRS. To investigate this, we used the proposed multipath extraction method to separate atmospheric errors from multipath errors, extracting multipath components for each satellite under both SRTK and SVRS. We then computed the standard deviation (STD) of each satellite's multipath errors, as illustrated in Fig. 9, which is now unaffected by atmospheric errors. The dashed lines represent the mean STD value of all satellites. The results show that SRTK's phase and pseudorange multipath values exceed those of SVRS by an average of 0.12 cm and 0.13 m. This suggests that the

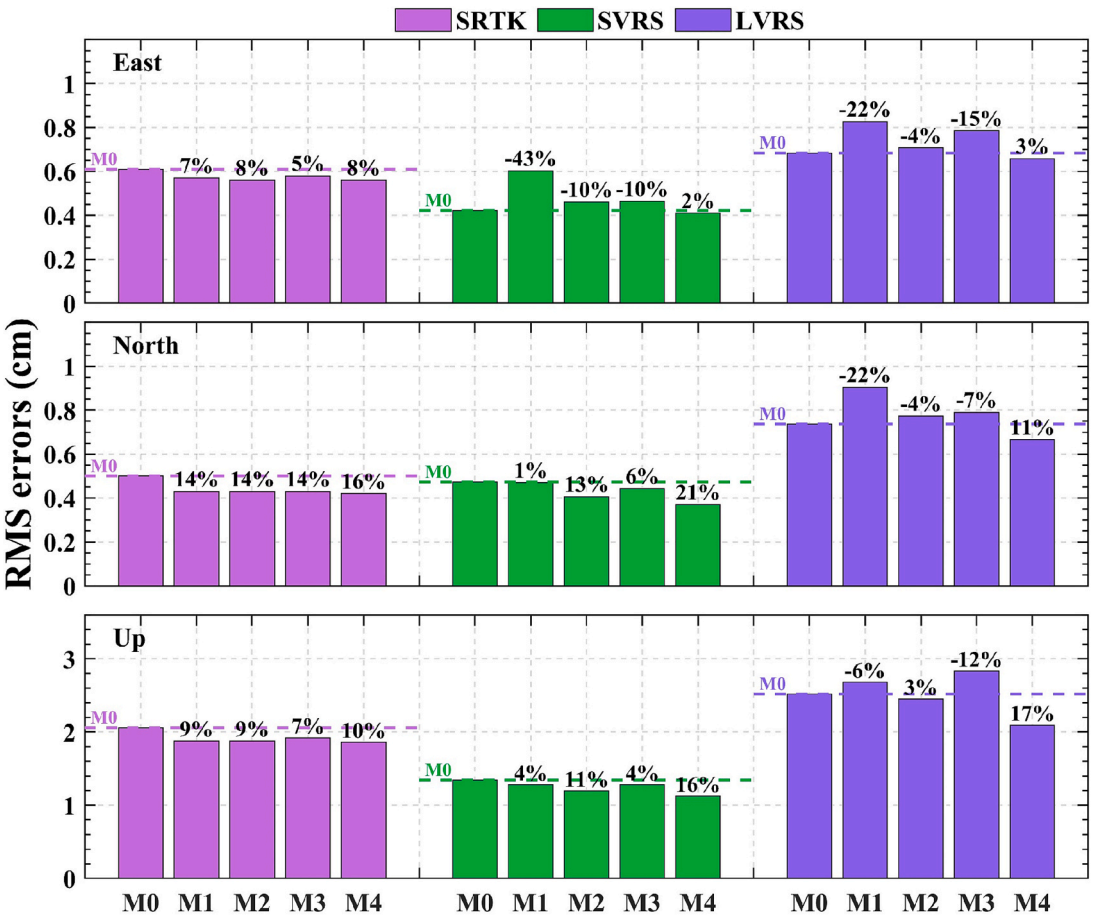

Fig. 8. RMS positioning errors at station SA02 on DOY 8 under three schemes (SRTK, SVRS, LVRS), before and after multipath correction with four mitigation methods (M1–M4).

reflection environment around the baseline reference station (REFE) in the SRTK scenario is more severe than that of the virtual reference station used in SVRS. A 0.12 cm difference in phase multipath can be interpreted as having a strong reflector placed near the station [37]. This observation aligns with Fig. 2(c), which shows dense tree coverage around REFE.

To further investigate the respective contributions of atmospheric and multipath errors to observation residuals under different baseline lengths (SRTK, SVRS, and LVRS), we used GPS L1 and BDS B1 data from DOY 7 as a case study. Fig. 10 illustrates the relative energy ratio of multipath in both phase and pseudorange residuals for each satellite, calculated using Eq. (8), across the three baseline schemes, along with the average relative energy ratio for all satellites in the GPS and BDS constellations.

In the phase residuals, more than 95% of the SRTK residuals are dominated by multipath errors. By contrast, under the SVRS and LVRS schemes, the proportion of multipath in the residuals decreases significantly compared to SRTK. Moreover, as the baseline increases from SVRS to LVRS, the multipath ratio further declines, while the atmospheric error ratio increases. This observation explains why, in Fig. 8, the M2 and M3 correction methods perform less effectively under LVRS than SVRS. The heightened proportion of atmospheric errors in the phase residuals makes it challenging for M2 to offset atmospheric influences on the multipath model, while M3 struggles to accurately extract principal components when multipath is no longer dominant. Interestingly, in the pseudorange residuals, the multipath ratio under SRTK is noticeably lower than that under SVRS or LVRS, and the trend of decreasing multipath ratio with increasing baseline length no longer applies. A plausible explanation is that atmospheric modeling accuracy, relative to the magnitude of pseudorange residuals, remains sufficiently high to minimize atmospheric impacts under both SVRS and LVRS. Furthermore, because the environment around the SRTK reference station is heavily obstructed by trees, the variability in local reflection conditions across consecutive ORTs is greater [38,39], reducing the fraction of correlated multipath in the SRTK solution compared to SVRS and LVRS.

4. Discussions

4.1. Assessment of multipath model applicability

To evaluate the applicability of the multipath correction model under the NRTK mode, we adopted two strategies to assess its performance. Strategy 1: Use the data from the three days preceding the correction day to build the correction model. Strategy 2**:** Use the data from DOY 1 to DOY 3 to construct the multipath correction model, which is then applied to DOY 4 to DOY 15. Fig. 11 shows the positioning errors in the east, north, and up directions for DOY 4 to DOY 15 under the SVRS scheme at station SA02. It compares the original unfiltered against the correction results of the M2 and the M4 method for both strategies. In each subfigure, the numeric labels denote the average STDs of positioning errors for M2 and M4 under both strategies. As seen, neither M2 nor M4 exhibits any significant decline in correction performance as time progresses, regardless of the strategy used.

To investigate why the correction performance does not degrade over time, we extracted the multipath components for satellites G02, G05, and C06 across 15 days using the proposed method. We then computed the time-based cross-correlation of both the multipath and

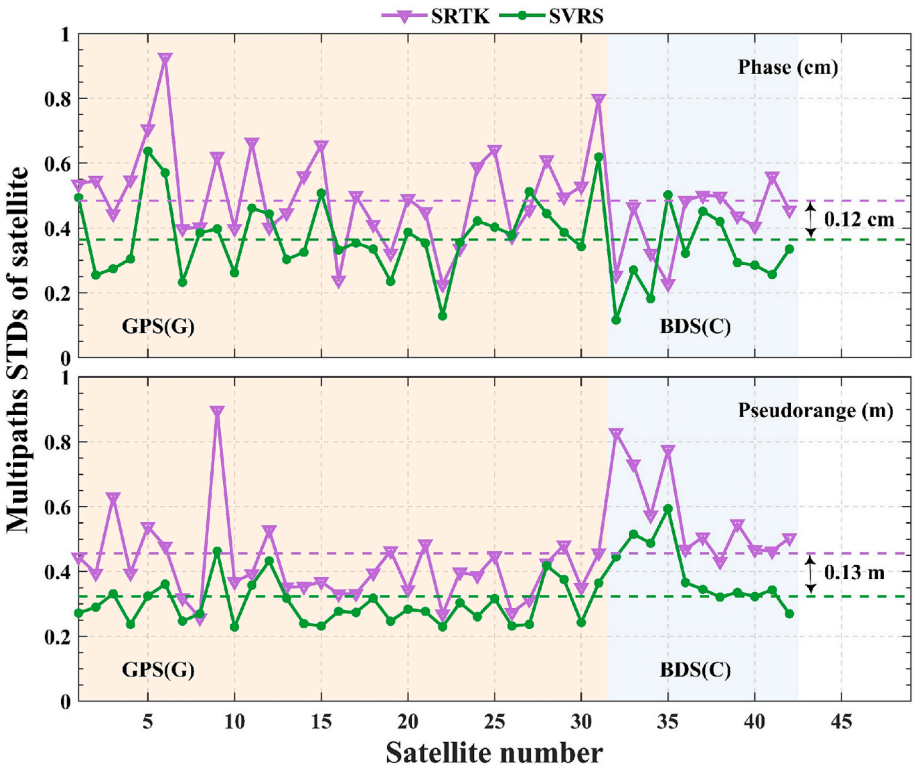

Fig. 9. STDs of multipath errors for all satellites at station SA02 on DOY 8 under SRTK and SVRS schemes, along with the overall mean STD (dashed line).

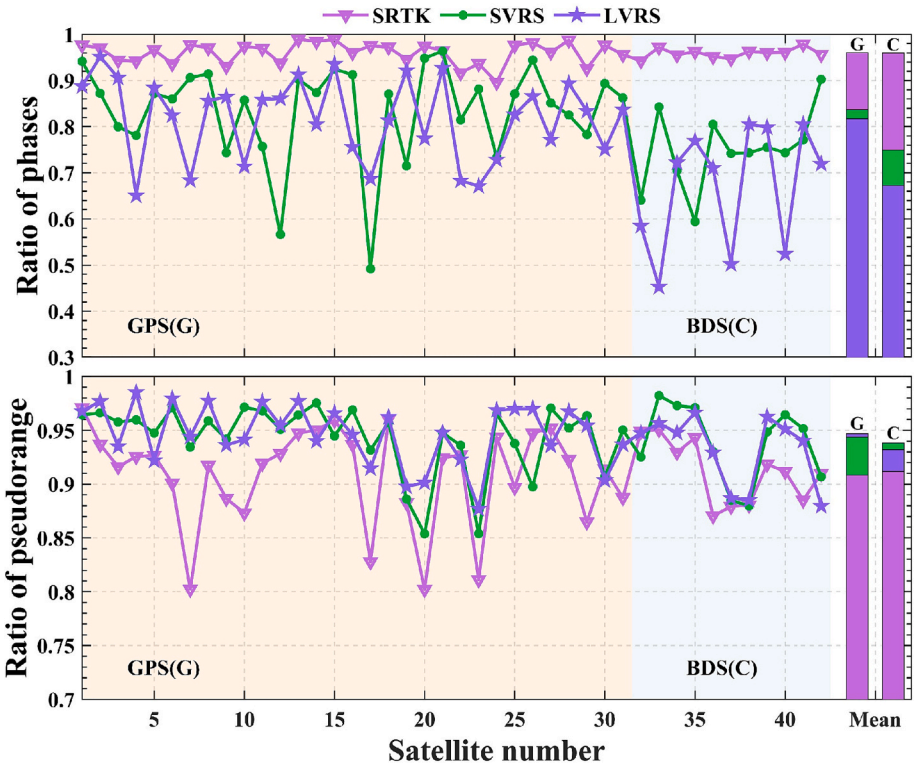

Fig. 10. Ratio of multipath eigenvalues to total eigenvalues for all satellites at station SA02 on DOY 7 under three baseline schemes (SRTK, SVRS, LVRS) at the L1/B1 frequency. Bar plots show the average ratios for the GPS (G) and BDS (C) constellations, respectively.

atmospheric errors. The results are presented in Fig. 12. It is evident that the multipath correlation for all three satellites does not diminish significantly over the 15-day span, suggesting that the multipath effect remains relatively stable over short periods (fewer than 15 days). Consequently, a multipath correction model built using M2 or M4 can be applied up to 12 days into the future without requiring a full rebuild. Nevertheless, as the lower panel of Fig. 12 reveals, the original SVRS residuals still contain low-frequency components that lack temporal

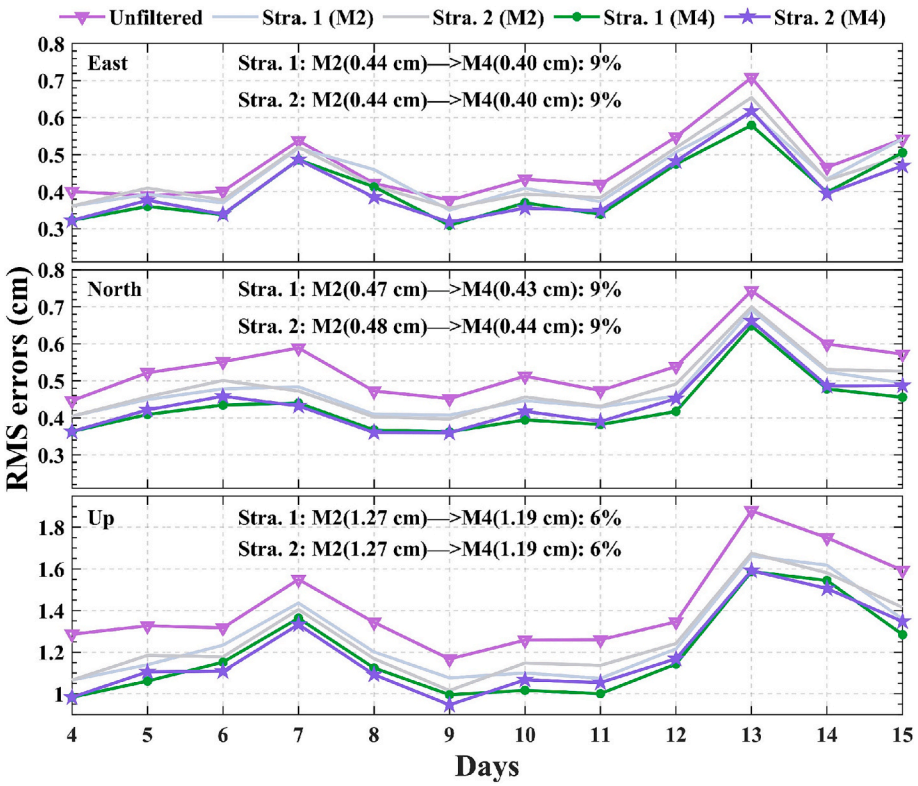

Fig. 11. East, north, and up positioning errors at station SA02 under the SVRS scheme for DOY 4 to DOY 15, comparing the unfiltered with the M2 and M4 (proposed) methods under two different modeling strategies.

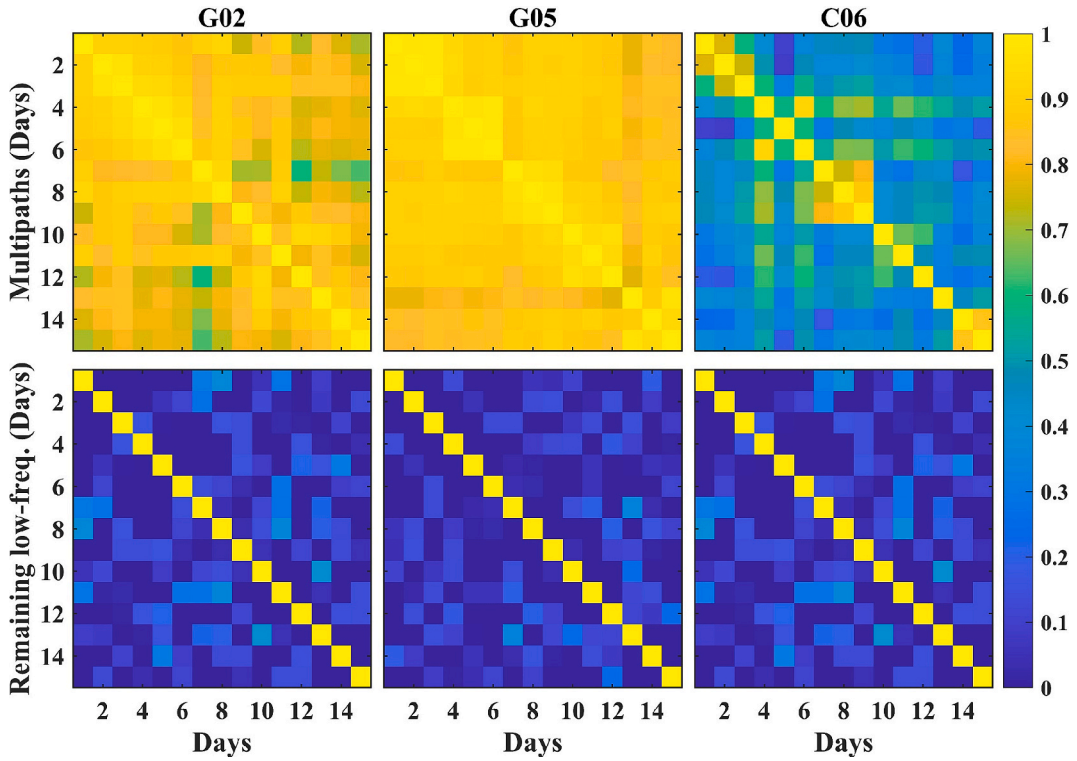

Fig. 12. Time-based cross-correlation of the extracted multipath errors (upper row) and the atmospheric errors (lower row) for satellites G02 (left), G05 (middle), and C06 (right) under SVRS from DOY 1 to DOY 15.

repeatability, and these components degrade the precision of traditional multipath correction approaches such as M2. This explains why, in Fig. 11, M4 outperforms M2. Compared to M2, the M4 approach improves the east, north, and up positioning accuracies by 9%, 9%, and

6%, respectively, and achieves 15%, 19%, and 16% improvements relative to the unfiltered data.

4.2. Rainfall-induced variations in multipath and atmospheric errors

We collected 2–hourly rainfall data from the Tsuen Wan District, the site of the landslide monitoring station. The proposed method was then applied to classify the low-frequency residuals of each satellite from DOY 1 to DOY 15 into multipath errors and remaining low-frequency components. Under the SVRS and SRTK schemes, the remaining low-frequency residuals can be interpreted as atmospheric errors and background noise [26], respectively. The daily average STDs of the multipath and remaining low-frequency residuals were computed across all satellites. For the SVRS scheme, the unfiltered RMS positioning errors in the up direction were also included to analyze their temporal behavior, as illustrated in Fig. 13. For clarity, the multipath and remaining low-frequency residuals were centralized, and the up-component RMS values were normalized to a comparable scale.

We categorized DOY 1 to DOY 8 as non-rainy days and DOY 10 to DOY 14 as rainy days, and calculated the average STDs for each period (dashed lines in Fig. 13). The results show that rainfall significantly increases both multipath errors and the remaining low-frequency residuals under both SVRS and SRTK. For multipath errors, one plausible explanation is that rainfall-induced increases in soil moisture enhance the ground attenuation coefficient [40,41], which strengthens multipath reflections. Under the SRTK, the multipath STD increases by 0.9 mm, slightly higher than the 0.7 mm increase under SVRS, reflecting differences in the surrounding environments of the reference stations.

Under the SVRS, the increased water vapor during rainfall also reduces the accuracy of the tropospheric delay model [42], leading to an atmospheric error increase of 0.4 mm between non-rainy and rainy periods. In contrast, the background noise under the SRTK exhibit little change, confirming that the double-differencing effectively eliminates tropospheric delay errors. Furthermore, it is evident that a short-duration heavy rainfall event (e.g., DOY 13) under the SVRS scheme sharply increased both multipath and atmospheric errors, resulting in reduced positioning accuracy.

5. Conclusions

Increasing baseline length leads to a higher proportion of atmospheric errors in the phase residuals. Conventional multipath correction models can inadvertently introduce these unmodeled atmospheric errors, degrading correction performance. In this study, we proposed a refined multipath modeling method that accounts for the effects of atmospheric errors and maintains robust accuracy across varying baselines. It improves the east, north, and up component positioning accuracies by about 9%, 9%, and 6%, respectively, compared to a standard three-day SF, and achieves roughly 15%, 19%, and 16% improvements relative to unfiltered data.

Heavy rainfall was observed to significantly increase both multipath errors and residual atmospheric errors, leading to reduced NRTK positioning accuracy during those periods. Since rainfall is a key trigger for landslides, such accuracy degradation poses a potential challenge for high-precision GNSS monitoring in adverse weather conditions. Further analysis of rainfall-induced error variations and the performance of the proposed method under different observation environments will be carried out in future work.

Machine-learning-based GNSS multipath modeling is a promising research direction, but it requires reliable features and, in particular, accurate multipath labels for supervised training. The proposed method provides cleaner multipath estimates that can serve as high-quality labels, facilitating future integration with machine-learning models for NRTK applications.

6. Consent for publication

All authors approved the final manuscript and the submission to this journal.

CRediT authorship contribution statement

Xinrui Li: Writing – original draft, Software, Methodology, Formal analysis, Conceptualization. **Xuanyu Qu:** Writing – review & editing, Supervision, Software, Methodology, Funding acquisition, Formal

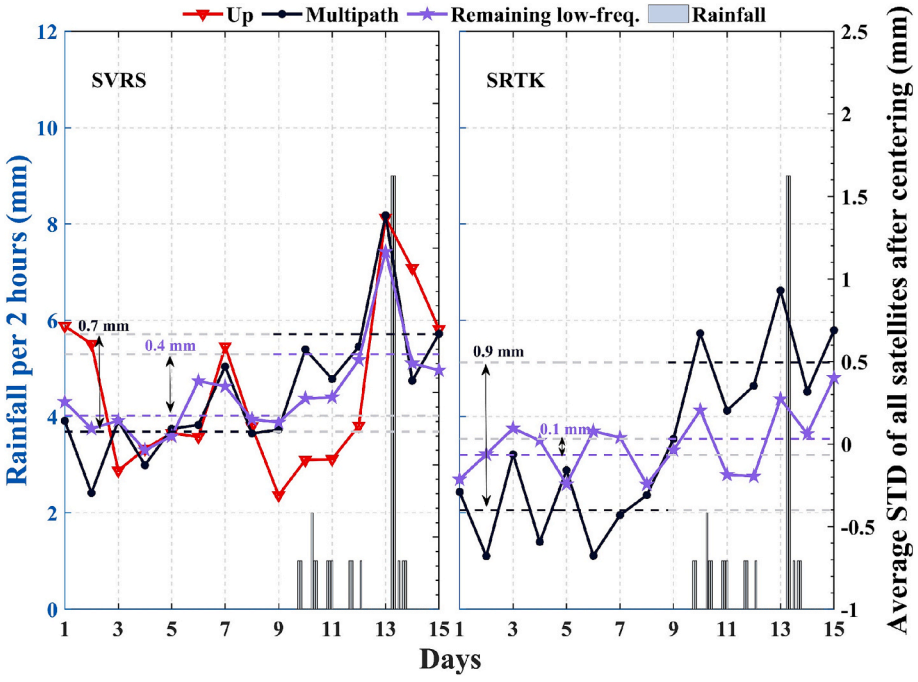

Fig. 13. Long-term relationship among multipath errors, remaining low-frequency errors, and rainfall under SVRS and SRTK schemes. Coloured dashed lines represent average values over non-rainfall and rainfall periods, respectively. The Up direction values are normalized to match the scale of the multipath errors.

analysis, Data curation, Conceptualization. **Xiaoli Ding:** Writing – review & editing, Supervision, Funding acquisition, Formal analysis. **Wenkun Yu:** Writing – review & editing, Formal analysis. **Li Wang:** Writing – review & editing, Supervision.

Funding

This research was jointly supported by the National Science Foundation of China (42504050, 42330717), and the Research Grants Council (RGC) of the Hong Kong Special Administrative Region (152318/22E, 152344/23E), Innovative Technology Commission (ITC) (K-BBY1 – Smart Railway Technology and Applications), PolyU Postdoctoral Funding (1-W39A), and Guangdong-Hong Kong Joint Laboratory for Marine Infrastructure (2025B1212150001).

Declaration of competing interest

The authors declare that they have no known competing financial interests or personal relationships that could have appeared to influence the work reported in this paper.

Acknowledgments

This research was jointly supported by the National Science Foundation of China (42504050, 42330717), and the Research Grants Council (RGC) of the Hong Kong Special Administrative Region (152318/22E, 152344/23E), Innovative Technology Commission (ITC) (K-BBY1 - Smart Railway Technology and Applications), PolyU Postdoctoral Funding (1-W39A), and Guangdong-Hong Kong Joint Laboratory for Marine Infrastructure (2025B1212150001).

Data availability

GNSS observation data were downloaded from the from the Hong Kong SatRef (https://www.geodetic.gov.hk/en/index.htm/). Rainfall data obtained from the Hong Kong Observatory (https://i-lens.hk/hkweather/daily_extract.php/).

References

[1] J. Malet, O. Maquaire, E. Calais, The use of global positioning system techniques for the continuous monitoring of landslides: application to the super-sauze earthflow (alpes-de-haute-provence, france), Geomorphology 43 (1–2) (2002) 33–54.
[2] K.M. Larson, P. Bodin, J. Gomberg, Using 1-hz GPS data to measure deformations caused by the denali fault earthquake, Science 300 (5624) (2003) 1421–1424, https://doi.org/10.1126/science.1084531.
[3] X. Qu, X. Ding, Y. Xia, W. Yu, A data-driven approach for analyzing contributions of individual loading factors to GNSS-measured bridge displacements, J. Geod. 98 (11) (2024), https://doi.org/10.1007/s00190-024-01913-7.
[4] X. Qu, X. Ding, W. Yu, et al., High-rate bridge displacement monitoring with low-rate virtual reference station data, GPS Solutions 29 (1) (2025) 8, https://doi.org/10.1007/s10291-024-01766-9.
[5] L. Wanninger, Real-Time Differential GPS Error Modelling in Regional Reference Station Networks, Springer, Berlin Heidelberg, 1998, pp. 86–92.
[6] Y. Bock, Continuous monitoring of crustal deformation, GPS World 2 (6) (1991) 40–47.
[7] T. Fuhrmann, X. Luo, A. Knöpfler, M. Mayer, Generating statistically robust multipath stacking maps using congruent cells, GPS Solutions 19 (1) (2015) 83–92, https://doi.org/10.1007/s10291-014-0367-7.
[8] D. Dong, M. Wang, W. Chen, et al., Mitigation of multipath effect in GNSS short baseline positioning by the multipath hemispherical map, J. Geod. 90 (3) (2016) 255–262, https://doi.org/10.1007/s00190-015-0870-9.
[9] K. Choi, A. Bilich, K.M. Larson, P. Axelrad, Modified sidereal filtering: implications for high-rate GPS positioning, Geophys. Res. Lett. 31 (22) (2004), https://doi.org/10.1029/2004GL021621.
[10] P. Zhong, X. Ding, L. Yuan, et al., Sidereal filtering based on single differences for mitigating GPS multipath effects on short baselines, J. Geod. 84 (2) (2010) 145–158, https://doi.org/10.1007/s00190-009-0352-z.
[11] M.R. Azarbad, M.R. Mosavi, A new method to mitigate multipath error in single-frequency GPS receiver with wavelet transform, GPS Solutions 18 (2) (2014) 189–198, https://doi.org/10.1007/s10291-013-0320-1.
[12] L. Lau, Wavelet packets based denoising method for measurement domain repeat-time multipath filtering in GPS static high-precision positioning, GPS Solutions 21 (2) (2017) 461–474, https://doi.org/10.1007/s10291-016-0533-1.
[13] X. Li, B. Shu, X. Qu, Q. Zhang, Y. Tian, G. Huang, L. Wang, Improving multipath extraction in PPP-RTK for high-precision dynamic deformation monitoring, Geospatial Inf. Sci. (2025) 1–14.
[14] X. Li, L. Wang, X. Qu, et al., A GPS multipath mitigation method in coordinate-domain considering the effects of gross errors and missing data, 225114035, Measurement (2024), https://doi.org/10.1016/j.measurement.2023.114035.
[15] Z. Wang, W. Chen, D. Dong, et al., Multipath mitigation based on trend surface analysis applied to dual-antenna receiver with common clock, GPS Solutions 23 (4) (2019) 1–15, https://doi.org/10.1007/s10291-019-0897-0.
[16] Z. Zhang, Y. Dong, Y. Wen, et al., Modeling, refinement and evaluation of multipath mitigation based on the hemispherical map in BDS2/BDS3 relative precise positioning, Measurement 213 (2023) 112722.
[17] Z. Zhang, L. Wang, X. Li, Characterization and modeling of GNSS site-specific unmodeled errors under reflection and diffraction using a data-driven approach, Satell. Navig. 6 (1) (2025) 8.
[18] B. Shu, Y. He, L. Wang, et al., Real-time high-precision landslide displacement monitoring based on a GNSS CORS network, 217113056, Measurement (2023), https://doi.org/10.1016/j.measurement.2023.113056.
[19] J. Geng, P. Jiang, J. Liu, Integrating GPS with GLONASS for high-rate seismogeodesy, Geophys. Res. Lett. 44 (7) (2017) 3139–3146, https://doi.org/10.1002/2017GL072808.
[20] J. Geng, Y. Pan, X. Li, et al., Noise characteristics of high-rate multi-GNSS for subdaily crustal deformation monitoring, J. Geophys. Res.-Solid Earth 123 (2) (2018) 1987–2002, https://doi.org/10.1002/2018JB015527.
[21] A. Hunegnaw, H. Duman, Y.G. Ejigu, et al., On the impact of GPS multipath correction maps and post-fit residuals on slant wet delays for tracking severe weather events, Atmos. 14 (2) (2023) 219, https://doi.org/10.3390/atmos14020219.
[22] K. Zheng, X. Zhang, J. Sang, et al., Common-mode error and multipath mitigation for subdaily crustal deformation monitoring with high-rate GPS observations, GPS Solutions 25 (2) (2021).
[23] D. Chen, S. Ye, F. Xia, et al., A multipath mitigation method in long-range RTK for deformation monitoring, GPS Solutions 26 (3) (2022), https://doi.org/10.1007/s10291-022-01281-9.
[24] R. Lu, M. Zhang, P. Yuan, et al., Enhancing multi-GNSS positioning performances in harsh environments via a refined joint troposphere-multipath hemispherical map, GPS Solutions 29 (1) (2025) 1, https://doi.org/10.1007/s10291-024-01763-y.
[25] W. Dai, D. Huang, C. Cai, Multipath mitigation via component analysis methods for GPS dynamic deformation monitoring, GPS Solutions 18 (3) (2014) 417–428, https://doi.org/10.1007/s10291-013-0341-9.
[26] L. Yu, Y. Gao, L. Jijian, et al., Improving GNSS-RTK multipath error extraction with an integrated CEEMDAN and STD-based PCA algorithm, GPS Solutions 28 (4) (2024) 192, https://doi.org/10.1007/s10291-024-01725-4.
[27] J. Yeh, J. Shieh, N.E. Huang, Complementary ensemble empirical mode decomposition: a novel noise enhanced data analysis method, Adv. Adapt. Data Anal. 02 (02) (2011) 135–156, https://doi.org/10.1142/S1793536910000422.
[28] P.C. Rodrigues, R. Mahmoudvand, The benefits of multivariate singular spectrum analysis over the univariate version, J. Franklin Inst.-Eng. Appl. Math. 355 (1) (2018) 544–564, https://doi.org/10.1016/j.jfranklin.2017.09.008.
[29] D. Odijk, H. van der Marel, I. Song, Precise GPS positioning by applying ionospheric corrections from an active control network, GPS Solutions 3 (3) (2000) 49–57, https://doi.org/10.1007/PL00012804.
[30] P.J. Teunissen, An optimality property of the integer least-squares estimator, J. Geod. 73 (11) (1999) 587–593.
[31] P. Zhong, X.L. Ding, D.W. Zheng, et al., Adaptive wavelet transform based on cross-validation method and its application to GPS multipath mitigation, GPS Solutions 12 (2008) 109–117.
[32] X. Qu, X. Li, L. Zheng, et al., A GNSS time series denoising method with mixed use of cross-validation and CEEMD-WT, Geomat. Inform. Sci. Wuhan Univ. 50 (12) (2025) 2440–2449, https://doi.org/10.13203/j.whugis20220570.
[33] H. Hassani, R. Mahmoudvand, Multivariate singular spectrum analysis: a general view and new vector forecasting approach, Int. J. Energy Stat. 1 (01) (2013) 55–83.
[34] M. Ghil, M.R. Allen, M.D. Dettinger, et al., Advanced spectral methods for climatic time series, Rev. Geophys. 40 (1) (2002), 3-1.
[35] S. Ye, D. Chen, Y. Liu, P. Jiang, W. Tang, P. Xia, Carrier phase multipath mitigation for BeiDou navigation satellite system, GPS Solutions 19 (4) (2015) 545–557.
[36] P. Wang, H. Liu, Z. Yang, et al., Evaluation of network RTK positioning performance based on BDS-3 new signal system, Remote Sensing 14 (1) (2021) 2.
[37] L. Lau, Investigations into the residual multipath errors of choke-ring geodetic antennas on GNSS carrier-phase measurements, GPS Solutions 29 (1) (2024) 42, https://doi.org/10.1007/s10291-024-01801-9.
[38] F. Moschas, S. Stiros, Dynamic multipath in structural bridge monitoring: an experimental approach, GPS Solutions 18 (2) (2014) 209–218, https://doi.org/10.1007/s10291-013-0322-z.
[39] H. Yuan, Z. Zhang, X. He, et al., Multipath mitigation in GNSS precise point positioning using multipath hierarchy for changing environments, GPS Solutions 27 (4) (2023), https://doi.org/10.1007/s10291-023-01531-4.

[40] P. Elosegui, J.L. Davis, Jaldehag, et al., Geodesy using the global positioning system; the effects of signal scattering on estimates of site position, J. Geophys. Res. 100 (B6) (1995) 9921–9934, https://doi.org/10.1029/95JB00868.
[41] K.M. Larson, J.J. Braun, E.E. Small, et al., GPS multipath and its relation to near-surface soil moisture content, IEEE J. Sel. Top. Appl. Earth Obs. Remote Sens. 3 (1) (2010) 91–99, https://doi.org/10.1109/JSTARS.2009.2033612.
[42] S. Bonafoni, R. Biondi, The usefulness of the global navigation satellite systems (GNSS) in the analysis of precipitation events, Atmos. Res. 16715–23 (2016), https://doi.org/10.1016/j.atmosres.2015.07.011.